

Kidney abnormality segmentation in thorax-abdomen CT scans

Gabriel Efrain Humpire Mamani¹, Nikolas Lessmann¹,
Ernst Th. Scholten¹, Mathias Prokop¹,
Colin Jacobs¹, Bram van Ginneken^{1,2}

¹*Diagnostic Image Analysis Group, Radboud University Medical Center,
Nijmegen, The Netherlands*

²*Fraunhofer MEVIS, Bremen, Germany*

`g.humpiremamani@radboudumc.nl`

Abstract

In this study, we introduce a deep learning approach for segmenting kidney parenchyma and kidney abnormalities to support clinicians in identifying and quantifying renal abnormalities such as cysts, lesions, masses, metastases, and primary tumors. Our end-to-end segmentation method was trained on 215 contrast-enhanced thoracic-abdominal CT scans, with half of these scans containing one or more abnormalities.

We began by implementing our own version of the original 3D U-Net network and incorporated four additional components: an end-to-end multi-resolution approach, a set of task-specific data augmentations, a modified loss function using top- k , and spatial dropout. Furthermore, we devised a tailored post-processing strategy. Ablation studies demonstrated that each of the four modifications enhanced kidney abnormality segmentation performance, while three out of four improved kidney parenchyma segmentation. Subsequently, we trained the nnUNet framework on our dataset. By ensembling the optimized 3D U-Net and the nnUNet with our specialized post-processing, we achieved marginally superior results.

Our best-performing model attained Dice scores of 0.965 and 0.947 for segmenting kidney parenchyma in two test sets (20 scans without abnormalities and 30 with abnormalities), outperforming an independent human observer who scored 0.944 and 0.925, respectively. In segmenting kidney abnormalities within the 30 test scans containing them, the top-performing method achieved a Dice score of 0.585, while an independent second human observer reached a score of 0.664, suggesting potential for further improvement in computerized methods.

All training data is available to the research community under a CC-BY 4.0 license on <https://doi.org/10.5281/zenodo.8014289>.

1 Introduction

Kidney cancer is a significant global health issue, ranking as the 12th most deadly cancer in the world, with an estimated 14,700 deaths in 2019 and approximately 73,820 new cases of kidney & renal pelvis cancer worldwide [30]. With the increasing number of cases, automated tools are needed to assist clinicians in managing this burden. For instance, by following nephrometry scoring systems [24], automatic kidney tumor segmentation methods may help specialists to detect and get reliable measurements of kidney tumors.

Previous research on kidney segmentation has employed a variety of conventional methods such as region growing [25, 22], active shape models [27], active contours [26, 31], graph cut[1, 38], level-sets[34, 2], snakes[9], random forest[21], and watersheds[36]. However, to the best of our knowledge, there are only a few methods that focus on segmenting kidney tumors or cysts in the literature. Linguraru et al. [26] proposed a semi-automatic method that combines fast marching and active geodesic contours to segment renal tumors. Kim and Park [22] used thresholds and histograms to segment the kidneys and applied texture analysis to the kidney parenchyma to find seeds for a region-growing algorithm to perform kidney tumor segmentation. Chen et al. [6] proposed a method to predict kidney tumor growth in mm^2/day , manually segmenting the kidney tumors and using a reaction-diffusion model to predict their growth. Kaur et al. [20] proposed an iterative segmentation method for renal lesions, which uses spatial image details and distance regularization.

In recent years, Convolutional Neural Networks (CNN) have shown to be more effective than traditional methods based on classical computer vision techniques and machine learning. Their ability to learn directly from raw data has led to their widespread use in segmenting organs and structures in different modalities. For instance, Zheng et al. [40] used an AlexNet-based method to localize the kidneys to define a seed for an active shape model algorithm to segment the kidneys in patients with either abdominal surgery or kidney tumors. Sharma et al. [29] used a network that takes the first 10 layers of the VGG-16 network and upsampled them in a decoder fashion to segment the kidneys of patients with renal insufficiency. Encoder-decoder networks such as 2D U-Net [28] and 3D U-Net [8] proved to be robust to tackle medical segmentation tasks in multiple medical imaging segmentation challenges [4, 18]. Variants of these models have been extensively proposed and applied to a wide variety of tasks, including kidney segmentation. For instance, Taha et al. [32] segmented the artery, vein, and ureter around the kidneys using a 2D U-Net-like network that allows the deeper layers to influence more to the final prediction. Jackson et al. [19] used a 3D U-Net-like network to segment the kidneys. Moreover, several methods used deep learning to segment kidney tumors [39, 37]. Yu et al. [39] proposed Crossbar-Net, a network that segments kidney and kidney tumors and uses horizontal and vertical patches instead of traditional squared patches. The network is divided into sets of sub-networks; a set consists of a sub-network for vertical and another for horizontal patches. Yang et al. [37] proposed a 3D CNN using a pyramid pooling module to segment the kidneys and kidney tumors in

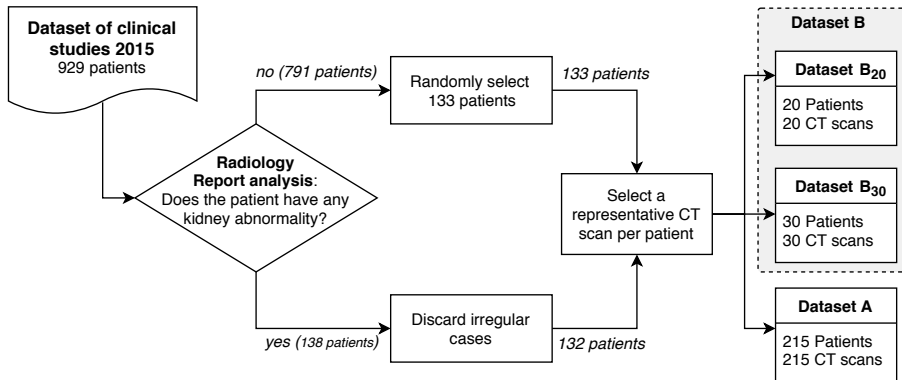


Figure 1: Diagram of the CT scans selection criteria for this study, with dataset A for training and datasets B₃₀ and B₂₀ for testing (with and without kidney abnormalities respectively).

abdominal CT angiographic scans.

The top competitors of the Medical Decathlon [18] and LiTS challenge [7, 14] have achieved the highest performance using cascaded networks. These networks divide the tasks into sub-tasks, with one network per sub-task. These networks have different fields of view and thus complement each other, resulting in higher performance. For instance, a first network may segment the liver and the liver tumor as a single structure, aiming to determine the region of interest for the second network; the second network then aims to segment the liver tumor class only. Similarly, Blau et al. [5] used cascade networks to segment the kidney and kidney cyst in CT scans using a 2D U-Net. Their method used heuristics such as a distance transform and HU thresholding to select cyst candidates within the kidney region. A second (shallow) network classified whether a candidate represented a kidney cyst. Additionally, Haghighi et al. [13] used a localization network for pre-processing, which cropped the input for 3D U-Net to segment MRI images of the kidneys. In a recent challenge on segmentation of the kidney and kidney tumors on CT [17], nnUNet [18] was the best performing method. This method automatically adapts its hyperparameters based on a fingerprint of the data, resulting in optimal performance. Furthermore, it uses 5-fold cross-validation to obtain the final prediction.

In this study, we propose an automatic method for segmenting the kidney parenchyma and kidney abnormalities in thorax-abdomen CT scans and compare it with the nnUNet. We trained our method on 215 thorax-abdomen CT scans and tested on additional 50 scans; the dataset consisted of scans from patients undergoing oncological workup. The dataset contains patients at different stages of disease and therefore abnormalities can be present in multiple body regions.

2 Materials and Methods

2.1 Patient Data

The dataset used in this study was collected from the Radboud University Medical Center, Nijmegen, the Netherlands. We randomly retrieved 1905 studies from 929 patients referred by the oncology department in a 12 month period. These patients did not opt-out for use of their data for research, Protected health information was removed from the DICOM data. This retrospective study was approved by the medical-ethical review board of the hospital. CT scanners from two manufacturers were used to acquire the CT scans: Toshiba (Aquilion One) and Siemens (Sensation 16, Sensation 64, and Somatom Definition AS). The reconstruction kernels were FC09, FC09-H, B30f, B30fs, and I30f. The slice thickness ranged from 0.5 to 3 millimeters, 90% of them between 1 and 2 mm. Severe abnormalities throughout the body are present in this dataset resulting from disseminated disease, surgery, chemotherapy, radiotherapy, etc.

We selected a subset to perform our experiments; the procedure is summarized in Figure 1. We analyzed the radiology reports per study to intentionally select potential cases that contain kidney abnormalities such as cysts, lesions, masses, metastases, and tumors. In Dutch: (*‘cyste’ OR ‘cysten’*), (*‘laesie’ OR ‘lesies’*), *‘massa’*, (*‘metastase’ OR ‘metastasen’*), and *‘tumor’*). Our selection criteria selected studies where the radiology report mentioned in the same sentence the kidneys (*‘nier’ OR ‘nieren’ NO ‘bijnier’*) and any kidney abnormalities. Furthermore, only one clinical study per patient was selected to get a large variety of anatomies for the segmentation task. In case multiple studies for the same patient were found, we selected the study with the earliest acquisition date.

We employed a radiology report analysis to curate a dataset of 138 clinical studies from 138 patients with kidney abnormalities, including cysts, lesions, masses, metastases, or tumors. We excluded six patients with unusual anatomy, three patients who had received kidney transplants, two patients with kidneys of irregular size, and one patient with a horseshoe kidney. The inclusion and exclusion criteria gave us 132 cases for analysis, which were then balanced with additional 133 random patient studies without kidney abnormalities, for a total of 265 CT scans from 265 patients. The patient cohort contains 56% males; the average age was 60 years, and the age ranged from 22 to 84. We divided this set into 215 CT scans for training (dataset A) and 50 for testing (dataset B). The test set was further subdivided, with 60% (30/50) containing abnormalities (dataset B₃₀) and the remaining 40% (20/50) devoid of abnormalities (dataset B₂₀). The distribution of the five types of abnormalities (tumors, cysts, masses, lesions, and metastases) was proportional among the 30 cases in dataset B₃₀ (six cases per abnormality), which were randomly selected.

In the test set, two and six patients had undergone left and right nephrectomy, respectively, while the training set included seventeen and eighteen patients who had undergone left and right nephrectomy, respectively.

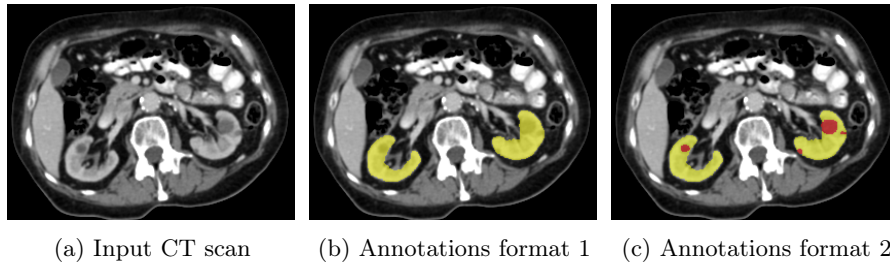
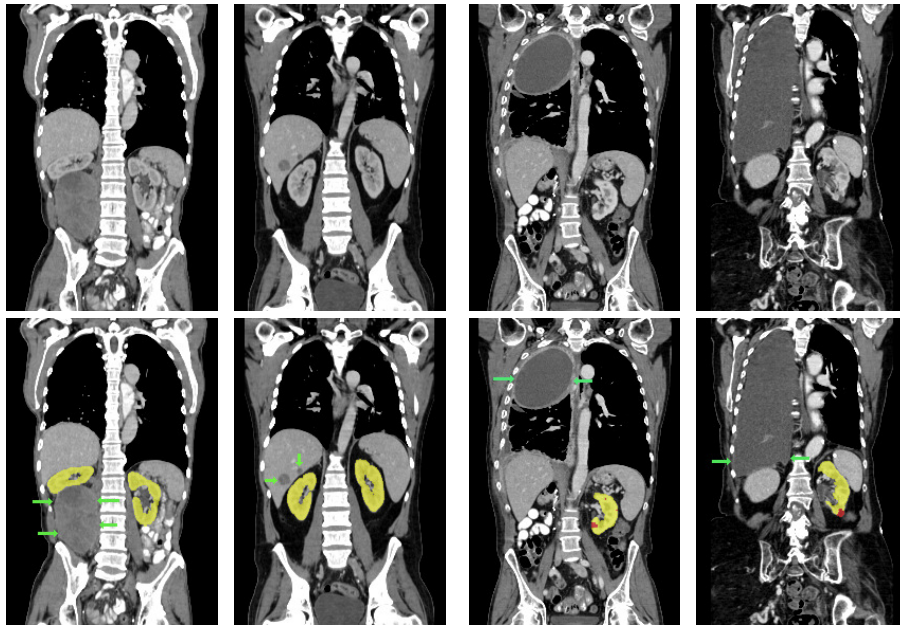


Figure 2: Example illustrating the different annotation formats. Each subfigure shows the same axial section, with overlays depicting the annotations: (a) shows the axial CT section. (b) shows the annotations in format 1: parenchyma and kidney abnormalities as a single structure (yellow overlay). (c) shows the annotations in format 2: parenchyma (yellow overlay) and kidney abnormalities (red overlay) as different structures. All images have a window center of 60 HU and a window width of 360 HU.

2.2 Annotation procedure

Four medical students manually segmented the kidney’s parenchyma and kidney abnormalities. They were trained by an experienced radiologist (EthS) and consulted the radiologist whenever needed throughout the annotation process. Adhering to a standardized protocol, the medical students annotated the kidney parenchyma as the region composed of the renal cortex, renal medulla, and renal pyramid. The renal hilum, collecting system, and (major and minor) calyces were excluded as much as possible from the kidney parenchyma annotations. We grouped cysts, lesions, masses, metastases, and tumors connected to the kidney parenchyma as kidney abnormalities. The protocol excluded cases with abnormalities in the collecting system.

Annotators used an in-house tool based on MeVisLab [15] to fully delineate the contours of the structures in 2D orthogonal planes. Our tool was designed to reduce the manual annotation time by interpolating unannotated contours between two manually delineated contours. The kidney parenchyma of the training set was annotated using an active learning process, with medical students correcting the kidney parenchyma predictions made by a pre-trained 3D U-Net (it used 50 CT scans from dataset A); the kidney abnormalities were annotated from scratch. The test set was manually annotated (i.e. the contour interpolation option of our tool was disabled) by two medical students. One of these was considered as the reference standard and the other one as the second observer ■. The latter was the most experienced among the medical students and was not allowed to consult the experienced radiologist during these annotations. The annotations of the second observer ■ served as a benchmark for human performance. The annotations were initially obtained in the axial plane, followed by corrections in coronal and sagittal planes to keep the annotation consistent in all orthogonal directions.



(a) Patients without kidney abnormalities. (b) Patients with kidney abnormalities.

Figure 3: Four examples of CT scans from the training set (dataset A) showing coronal sections with annotations in format 2 (see Figure 2c) where yellow and red overlays represent annotations of the parenchyma and kidney abnormalities, respectively. Note that all the patients have anomalies in the body (green arrows in the body), and both cases of (b) have only one kidney and contain kidney abnormalities. All the slices have a window center of 60 HU and a window width of 360 HU.

This study utilized two annotation formats, format 1 and format 2, to store the annotations. Format 1 considers the kidney parenchyma and kidney abnormalities as a single class (see Figure 2b) while format 2 separates them into two classes (see Figure 2c).

Samples of CT scans from patients included in this study can be seen in Figure 3. While Figure 3a depicts patients without kidney abnormalities, it highlights the presence of abnormalities in other parts of the body, such as liver tumors. Figure 3b shows patients with kidney abnormalities, as well as other abnormalities in the body, such as nephrectomy and collapsed lung.

2.3 Segmentation network

We present an end-to-end method for segmenting renal parenchyma and abnormalities in CT scans. We depict our architecture in Figure 4. It consists of two segmentation networks, a multi-resolution network for kidney segmentation

(annotations in format 1, one voxel represents $4\times 4\times 4\text{mm}$) and a high-resolution network (annotations in format 2, one voxel represents $1\times 1\times 1\text{mm}$). The multi-resolution network is designed to first provide a rough localization of the kidney by processing a low-resolution version of the CT scan. This defines an ROI for the high-resolution network to refine the segmentation of the kidneys and kidney abnormalities.

2.3.1 Pre-processing

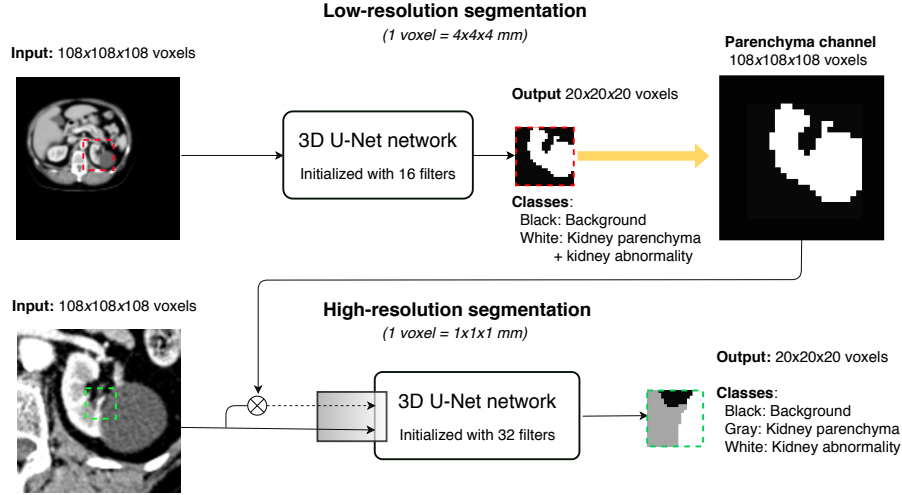
The CT scans and annotations were resampled to $1\times 1\times 1\text{mm}$ (for high-resolution segmentation using annotations in format 2) and $4\times 4\times 4\text{mm}$ (for multi-resolution segmentation using annotations in format 1) resolutions (see Figure 4a). Scans and annotations were resampled using cubic and nearest-neighbor interpolation, respectively. We clipped the Hounsfield Units to the range $[-500,400]$.

2.3.2 Multi-resolution network

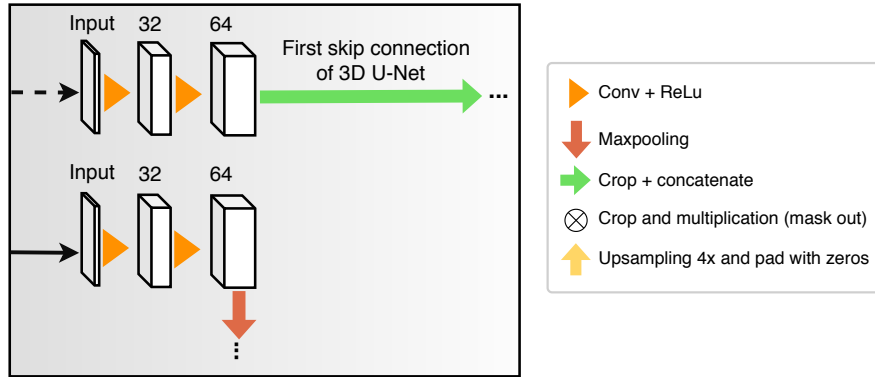
We present an end-to-end cascade method for parenchyma and kidney abnormality segmentation. Unlike traditional cascade networks, which use two separate networks and do not allow for backpropagation, our approach uses a single network composed of two sub-networks. The first sub-network is a 3D U-Net with 16 filters that performs multi-resolution segmentation and defines an ROI. This network takes 3D patches of $108\times 108\times 108$ voxels, with each voxel representing $4\times 4\times 4\text{mm}$, as input using annotations in format 1 (kidney parenchyma + kidney abnormalities) and outputs $20\times 20\times 20$ voxels. The output is then up-sampled 4 times and padded with zeros to match and mask out the high-resolution input image in millimeters ($108\times 108\times 108\text{mm}$, one voxel represents $1\times 1\times 1\text{mm}$). The masked-out image serves as an additional input to the second sub-network, the high-resolution segmentation network, which uses a 3D U-Net with 32 filters and serves to fine-segment the kidneys and kidney abnormalities (see Figure 4b). Figures 4a and Figure 4b illustrate our approach and the connection between the multi-resolution and the high-resolution segmentation network, respectively.

2.3.3 Data augmentation

Data augmentation was applied randomly to 70% of the training samples using scaling, rotation, Gaussian blurring, image intensity variation, and elastic deformation. Up to three of these data augmentation methods were applied randomly to each training sample, to prevent too much data distortion. When elastic deformation was used, it was only performed in conjunction with Gaussian blurring and image intensity variation. Interpolation methods of cubic and nearest neighbor were used for CT scans and reference standards, respectively. The scaling factor ranged from 0.95 to 1.05, with rotations of up to two planes of -5° to 5° degrees. Gaussian blurring had a sigma range of 0.2 to 1.0, and image intensity variation varied between -20 and 20 HU. We performed elastic deformation by placing ten control points in a grid, randomly perturbed by up to 5 voxels that were used as input to cubic B-spline interpolation.



(a) Diagram of the proposed multi-resolution network.



(b) Input of the high-resolution segmentation.

Figure 4: (a) Diagram of the proposed network. The multi-resolution segmentation network uses a 3D U-Net network initialized with 16 filters. It processes blocks of $108 \times 108 \times 108$ voxels and outputs the central $20 \times 20 \times 20$ voxels (represented by the dashed red square). One voxel corresponds to a resolution of $4 \times 4 \times 4$ mm, giving the network a receptive field of $88 \times 88 \times 88$ voxels or $352 \times 352 \times 352$ mm. The kidney parenchyma and kidney abnormalities are considered a single class in the multi-resolution network (see Figure 2b). The high-resolution segmentation network uses a 3D U-Net architecture initialized with 32 filters, with each voxel representing $1 \times 1 \times 1$ mm. Its receptive field is $88 \times 88 \times 88$ mm and it segments the parenchyma and the kidney abnormalities as different classes (see Figure 2c). (b) Shows how the multi-resolution and the high-resolution networks are connected.

2.3.4 Spatial dropout

We applied spatial dropout [33], a regularization technique that is different from traditional dropout. Spatial dropout drops feature maps instead of individual neurons to enforce independence among feature maps, encouraging the network to learn more robust and generalizable features. We randomly dropped 10% of the feature maps per layer.

2.3.5 Loss function

The loss function determines how the network’s weights are optimized after a forward pass. In our experiments, we used a combination of weighted categorical cross-entropy and dice loss in the experiments.

$$\text{Combined loss} = \alpha * \text{diceLoss} + \gamma * \text{TopK}(\text{weightedCrossentropy}) \quad (1)$$

where $\alpha = 0.3$ and $\gamma = 0.7$ were used in all the experiments. Top- k [3] sorts the voxel-wise loss in descending order and keeps the top $k\%$ to compute the final mean loss; this approach emulates an online voxel-wise hard-mining per sample.

2.3.6 Post-processing

The output of the networks was post-processed to eliminate false positives. The end-user prediction was reconstructed by stitching together the predictions. In all the networks, the output was thresholded at 0.5 to get a binary prediction. The predictions of the multi-resolution network were up-sampled four times and dilated five times to mask out the predictions of the high-resolution segmentation network. Only the kidney abnormalities that were connected to the kidney parenchyma were kept, to ensure that there were no spurious kidney abnormality candidates outside the kidney region.

2.3.7 CNN Settings

Due to the large footprint of the network, scans were divided into 3D patches to train the 3D network. Each training sample consisted of a patch of $108 \times 108 \times 108$ voxels from the CT scan and a $20 \times 20 \times 20$ voxel reference standard. During training, the reference standard patches were sampled every ten voxels in all the orthogonal planes with up to 50% overlap among surrounding patches. During inference, the cubes do not overlap. Patches at the border of the CT scan were mirrored to match the input network size.

The Glorot uniform algorithm [12] was used to initialize the weights of the network. The weight-map w compensated for the high-class imbalance between the classes. The background, parenchyma, and kidney abnormality classes had empirically defined weights of 0.05, 0.10, and 0.99, respectively. We used Adam [23] as optimization function with learning rate= 0.00001, $\beta_1 = 0.9$, and $\beta_2 = 0.999$. The training stopped when the performance on the validation set stopped improving for ten epochs, and the model with the highest average Dice score on the validation set was selected as the optimal model.

2.3.8 Implementation of the CNN

The networks were implemented using Keras and TensorFlow as backend in Python 3.6. The segmentation experiments were executed on a cluster of computers equipped with GTX1080 and GTX1080ti graphics cards, each with 256GB of CPU RAM.

2.4 Evaluation

The end-user segmentation obtained by our networks was compared to the reference masks using the Dice score.

$$\text{Dice score} = \frac{2 * \text{volume}(X \cap Y)}{\text{volume}(X) + \text{volume}(Y)} \quad (2)$$

where X is the prediction, and the Y is the reference standard.

2.5 Ablation study

In this section, we conducted a step-by-step evaluation of the impact of each module (multi-resolution, data augmentation, top-k, and spatial dropout) in our proposed network. The backbone architecture for this ablation study was the 3D U-Net [8]. Our experiments setup started with a 3D U-Net, and additional modules were added one by one in subsequent experiments (see the left side of Table 1). In order to evaluate the impact of each module on the network performance, we conducted an ablation study by adding modules to the 3D U-Net backbone architecture one by one. The baseline network, referred to as experiment 5 ■, only used the 3D U-Net initialized with 32 filters and had a single input of $108 \times 108 \times 108$ voxels with $1 \times 1 \times 1$ mm per voxel, producing $20 \times 20 \times 20$ voxels. The subsequent experiments added the multi-resolution module (experiment 4 ■), data augmentation module (experiment 3 ■), top- k module (experiment 2 ■), and spatial dropout module (experiment 1 ■) to the network. The input and output sizes and formats were consistent across all experiments except experiment 5 ■; networks receive two inputs of $108 \times 108 \times 108$ voxels each, one input of $1 \times 1 \times 1$ mm and one input of $4 \times 4 \times 4$ mm per voxel for high-resolution (input of $108 \times 108 \times 108$ mm using annotation format 2) and multi-resolution segmentation (input of $432 \times 432 \times 432$ mm using annotation format 1), respectively. The difference in performance between experiment 1 ■ (experiment with spatial dropout) and experiment 2 ■ (experiment without spatial dropout) showed the influence of the spatial dropout module, for example. As an initial step, we first trained the multi-resolution module independently to reach its optimal sub-model. Afterward, we froze the weights of the multi-resolution sub-model, except for the last three layers to allow back-propagation from the high-resolution segmentation network. All the experiments used 80% of dataset A for training and 20% for validation. Each experiment was trained independently to find the optimal model. The best model from each experiment was evaluated using test sets B_{20} and B_{30} .

2.6 nnUNet

We conducted experiments with nnUNet [18] to compare its performance with our methods. Unlike our approach, nnUNet processes CT scans without any preprocessing step, while we resample the CT scans to an isotropic resolution and clip the HU range. To gain insight about the benefits of ensemble networks, we ensembled nnUNet with our two highest-performing methods, one at a time. As nnUNet only uses thresholding as postprocessing, we analyzed the impact of our dedicated postprocessing method on performance. Note that our postprocessing eliminates false-positive kidney abnormalities that are not attached to the parenchyma.

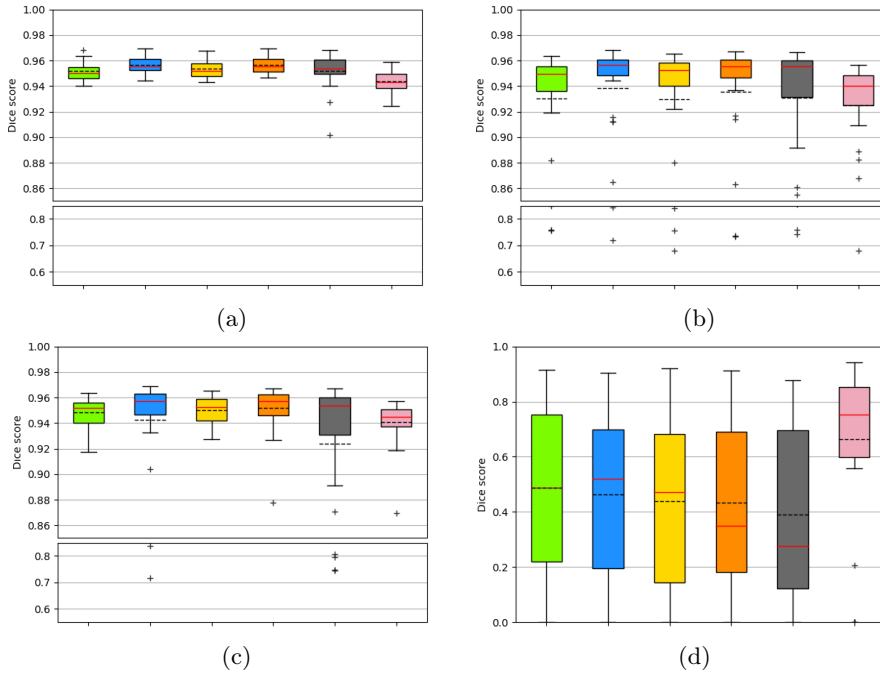


Figure 5: Performance comparison of our methods and the second observer ■ on datasets B_{20} and B_{30} using boxplots. The red and black lines represent the median and the mean, respectively. Boxplot (a) shows results for class parenchyma only on the dataset B_{20} (twenty cases without abnormalities). Boxplot (b) shows results for class parenchyma only on the dataset B_{30} (thirty cases with abnormalities). Boxplot (c) displays the results for class parenchyma plus abnormalities as a single structure on dataset B_{30} (thirty test cases with abnormalities). Boxplot (d) shows results for Class abnormalities only on the dataset B_{30} (thirty cases with abnormalities). Note that the scale in the y-axis is different for boxplot (d). The modules for each experiment are represented by the same color coding as in Table 1: experiment 1 ■, experiment 2 ■, experiment 3 ■, experiment 4 ■, experiment 5 ■, and second observer ■.

3 Results

The results of the ablation study conducted on the test sets (dataset B_{20} and B_{30}) are shown in Figure 5. These results are also summarized in Table 1, which includes asterisks (*) to indicate statistical significance (P-value < 0.05) between experiment 1 ■ and other experiments, as determined by a two-tailed Mann-Whitney U test. We evaluated the predictions of each experiment per class to show more insights into the results of our experiments. Furthermore, we combined the prediction of both classes (annotation format 2) as a single structure (annotation format 1) and computed its Dice score; this helps to make our results comparable to methods that reported kidney dice only.

Dataset B_{30} : The presence of kidney abnormalities characterizes the patients in this dataset (see Figure 3b). The results of our experiments on dataset B_{30} are displayed in Figures 5d, 5b, and 5c. First, we evaluated the performance of the methods in segmenting the kidney abnormalities class only. The results are shown in Figure 5d and in the column “Dataset B_{30} /Abnormalities class” of Table 1. The second observer ■ and experiment 1 ■ achieved the two highest scores, 0.664 ± 0.274 and 0.487 ± 0.314 , respectively. Experiment 5 ■ obtained 0.390 ± 0.315 Dice, the lowest score when segmenting the kidney abnormalities only. Next, we evaluated the performance of the methods in segmenting the parenchyma class only. The results are shown in Figure 5b and in the column “Dataset B_{30} /Parenchyma class” of Table 1. The two highest scores were obtained by Experiment 2 ■ and experiment 4 ■ with 0.938 ± 0.051 , 0.936 ± 0.058 , respectively, while the second observer ■ obtained the lowest score with 0.925 ± 0.051 . Finally, we evaluated the performance of the methods when segmenting both the parenchyma and the kidney abnormalities class as a single structure (annotation format 1). The results are shown in Figure 5c and in column “Dataset B_{30} /Parenchyma + abnormalities class” of Table 1. The two highest scores were achieved by Experiment 4 ■ and experiment 3 ■ with Dice scores 0.952 ± 0.017 and 0.950 ± 0.010 , respectively. Experiment 5 ■ obtained the lowest Dice score with 0.924 ± 0.065 .

Dataset B_{20} : The patients in this dataset do not present kidney abnormalities, but it is probable that they have other anomalies in the body (see Figure 3a). The results on the test set B_{20} are depicted in Figure 5a and in Table 1 under the column “Dataset B_{20} /Parenchyma class”. Experiment 2 ■ and experiment 4 ■ obtained the highest Dice scores, 0.957 ± 0.006 and 0.956 ± 0.007 , respectively. The second observer ■ obtained the lowest Dice score with 0.944 ± 0.009 .

nnUNet: In our experiments, nnUNet obtained slightly better results in the parenchyma class of datasets B_{20} and B_{30} compared to our experiments, a Dice score of 0.521 ± 0.303 in the kidney abnormality class, which was higher by $+0.034$ Dice than our experiment 1 ■. To further analyze the differences between nnUNet and our experiments, we ensembled the predictions of nnUNet with either experiment 1 ■ or experiment 2 ■ by averaging their probabilities. The ensemble nnUNet with experiment 2 ■ slightly improved the results of nnUNet in the parenchyma class of both datasets but decreased in -0.014 Dice score in the abnormality class, while the ensemble nnUNet with experiment 1 ■ slightly

Table 1: Summary of performance of our methods and the second observer  on the test sets (dataset B₂₀ and B₃₀) using Dice score. The upper part of the table shows Mean and SD, while the bottom part shows 95% Confidence Intervals. We analyzed the performance per class (parenchyma and kidney abnormalities) and when both classes are combined (parenchyma + kidney abnormalities). An asterisk (*) indicates that a value is significantly better or worse than the value of the reference system (experiment 1 ). The best Dice score values per column are in bold.

Experiment	Test set: dataset B ₂₀		Test set: dataset B ₃₀	
	Parenchyma class (Fig. 5a)	Parenchyma class (Fig. 5b)	Parenchyma + abnormalities class (Fig. 5c)	Abnormalities class (Fig. 5d)
	<i>Mean ± SD</i>			
Exp. 1 	0.952±0.008	0.930±0.053	0.948±0.011	0.487±0.314
Exp. 2 	*0.957±0.006	*0.938±0.051	*0.942±0.049	0.464±0.320
Exp. 3 	0.954±0.007	0.930±0.064	0.950±0.010	0.440±0.310
Exp. 4 	*0.956±0.007	0.936±0.058	*0.952±0.017	0.434±0.311
Exp. 5 	0.952±0.015	*0.931±0.057	*0.924±0.065	0.390±0.315
Second observer 	*0.944±0.009	*0.925±0.051	*0.941±0.017	0.664±0.274
nnUNet	*0.960±0.015	*0.940±0.069	*0.931±0.099	0.521±0.303
Ens. nnUNet Exp. 1 	*0.962±0.007	*0.941±0.058	*0.927±0.125	0.526±0.305
Ens. nnUNet Exp. 2 	*0.964±0.006	*0.944±0.055	*0.928±0.129	0.507±0.318
nnUNet PP	*0.964±0.006	*0.941±0.068	*0.955±0.042	0.576±0.290
Ens. nnUNet Exp. 1 	*0.962±0.007	*0.942±0.058	*0.960±0.009	0.585±0.293
Ens. nnUNet Exp. 2 	*0.965±0.006	*0.947±0.050	*0.958±0.032	0.566±0.309
<i>Confidence Intervals 95%</i>				
Exp. 1 	0.948-0.955	0.910-0.950	0.945-0.952	0.369-0.604
Exp. 2 	0.954-0.960	0.920-0.957	0.924-0.961	0.345-0.584
Exp. 3 	0.950-0.957	0.906-0.954	0.946-0.954	0.324-0.555
Exp. 4 	0.953-0.959	0.914-0.957	0.945-0.958	0.318-0.550
Exp. 5 	0.945-0.959	0.910-0.952	0.900-0.948	0.273-0.508
2nd observer	0.939-0.948	0.906-0.944	0.935-0.947	0.561-0.766
nnUNet	0.953-0.965	0.913-0.961	0.892-0.959	0.411-0.625
Ens. nnUNet Exp. 1 	0.959-0.965	0.918-0.958	0.876-0.959	0.416-0.627
Ens. nnUNet Exp. 2 	0.961-0.967	0.923-0.961	0.876-0.961	0.397-0.613
nnUNet PP	0.961-0.967	0.915-0.962	0.938-0.965	0.469-0.673
Ens. nnUNet Exp. 1 	0.959-0.966	0.918-0.959	0.957-0.963	0.482-0.687
Ens. nnUNet Exp. 2 	0.962-0.967	0.926-0.963	0.945-0.965	0.454-0.672

improved in $+0.004$ dice score compared to nnUNet in the abnormality class. The ensemble nnUNet with experiment 2 ■ performed slightly better than the ensemble nnUNet with experiment 1 ■ in all classes, except the abnormality class, where the ensemble with experiment 1 ■ had a Dice score of 0.526 ± 0.306 , and the ensemble with experiment 2 ■ obtained 0.507 ± 0.318 . Since nnUNet only uses thresholding for post-processing, we applied our dedicated post-processing to the nnUNet predictions to remove kidney abnormalities that are not attached to the kidney, which resulted in notable improvements of $+0.055$, $+0.059$, and $+0.059$ for nnUNet, ensemble nnUNet with experiment 1 ■, and ensemble nnUNet with experiment 2 ■, respectively. As a result, the ensemble nnUNet with experiment 1 ■ and our dedicated post-processing was the highest-performing experiment in the abnormality class, with a Dice score of 0.585 ± 0.293 .

Table 2 compares our results with other methods published in the literature. Some of the methods report the Dice scores for the left and right kidneys separately, while others report a single score for both kidneys combined. To make our results comparable to these methods, we post-processed our predictions to obtain the Dice scores for both the left and right kidneys.

4 Discussion

In this paper, we presented an automatic method for the segmentation of the (kidney) parenchyma and kidney abnormalities. We conducted experiments in an ablation study fashion to evaluate the contribution of each module to the performance (see Section 2.5). For instance, the comparison between experiment 5 ■ and experiment 4 ■ in Figure 5 shows the influence of the multi-resolution module. Figure 5a shows that all of our experiments outperformed the second observer ■ when segmenting the kidney parenchyma in dataset B_{20} (patients without kidney abnormalities). While the presence of kidney abnormalities affected the performance of kidney (parenchyma + abnormalities) segmentation; see the difference of outliers between Figure 5a (dataset B_{20}) and Figure 5c (dataset B_{30} : patients with kidney abnormalities). One of the reasons for this behavior may be the difficulty in defining the boundary between the parenchyma and the kidney abnormality. When comparing the boxplots, the interquartile range of Experiment 5 ■ and experiment 2 ■ obtained the largest and the smallest interquartile range, respectively, indicating that the combination of multi-resolution, data augmentation, and top- k modules positively impacted the segmentation of the kidneys (parenchyma + abnormalities). Note the spatial dropout module (difference between experiment 1 ■ and experiment 2 ■) was beneficial only to the kidney abnormality class (see Figure 5). Furthermore, Figure 5d shows that the mean Dice score (black dashed line in boxplots) of our experiments gradually increases when adding more modules (experiment 5 ■ to experiment 1 ■) when segmenting the kidney abnormality class. This highlights the positive impact of each module in this ablation study on the segmentation of kidney abnormalities.

Table 2: Performance comparison between our methods (experiment 1 ■ and experiment 2 ■) and previous work of kidney segmentation and kidney tumor/abnormality segmentation using the mean Dice score as the metric. The methods listed below the line reported the presence of cases with kidney tumors/abnormalities in their datasets. The values marked with † are obtained after post-processing the prediction masks from 'Both kidneys' column for comparability with other methods.

Method	Kidney abnormality masks		Both kidneys	Num. test scans	Deep Learning	Description
	Left kidney	Right kidney				
<i>Methods that reported cases without kidney abnormalities or did not report them</i>						
Jackson et al. [19]	N/A	0.860	0.910	-	24	Yes
Gibson et al. [10, 11]	N/A	0.930	-	-	10	Yes
Badura and Wiclawek [2]	N/A	0.938	0.944	-	20	No
Heinrich et al. [16]	N/A	0.942	-	-	10	Yes
Wang et al. [35]	N/A	0.956	0.954	-	30	Yes
Khalifa et al. [21]	N/A	-	-	0.973	60	No
Exp. 1 ■	N/A	0.953†	0.951†	0.952	20	Yes
Exp. 2 ■	N/A	0.960†	0.955 †	0.957	20	Yes
Second observer ■	N/A	0.943†	0.945†	0.944	20	N/A
nnUNet	N/A	0.956†	0.959†	0.960	20	Yes
Ens. nnUNet Exp. 1 ■	N/A	0.962†	0.944†	0.962	20	Yes
Ens. nnUNet Exp. 2 ■	N/A	0.964 †	0.946†	0.965	20	Yes
<i>Methods that reported cases with kidney abnormalities</i>						
Turco et al. [34]	-	-	-	0.800	55	No
Sharma et al. [29]	-	-	-	0.860	81	Yes
Skalski et al. [31]	-	-	-	0.862	10	No
Blau et al. [5]	-	0.870	0.870	-	46	Yes
Lin et al. [25]	-	0.873	0.886	-	30	No
Zheng et al. [40]	-	0.890	0.920	-	78	Yes
Wiclawek [36]	-	-	-	0.917	170	No
Yang et al. [37]	0.802	-	-	0.931	50	Yes
Yu et al. [39]	0.913	-	-	-	36	Yes
Exp. 1 ■	0.488	0.949†	0.951†	0.948	30	Yes
Exp. 2 ■	0.464	0.956†	0.936†	0.942	30	Yes
Second observer ■	0.664	0.939†	0.943†	0.941	30	N/A
nnUNet	0.521	0.928†	0.951†	0.931	30	Yes
Ens. nnUNet Exp. 1 ■	0.585	0.960†	0.960 †	0.960	30	Yes
Ens. nnUNet Exp. 2 ■	0.566	0.963 †	0.955†	0.958	30	Yes

Additionally, we trained nnUNet, a state-of-the-art segmentation method, on our data and obtained results that were consistent with our previous experiments, except for the kidney abnormality class where nnUNet achieved a 0.521 Dice score compared to 0.488 obtained by experiment 1 ■. To explore further improvements, we combined nnUNet predictions with our best-performing experiments, resulting in an ensemble nnUNet + experiment 1 ■ that achieved 0.526 Dice score for the kidney abnormality class. Since nnUNet uses only thresholding as postprocessing, we investigated whether postprocessing nnUNet predictions with our dedicated postprocessing could result in better performance. This additional postprocessing yielded a 0.585 Dice score, an improvement of +0.064 compared to the original nnUNet with 0.521 Dice score. While nnUNet is a state-of-the-art segmentation method, our dedicated postprocessing method contributed to further improvement in discarding false positive regions.

We note that the performance of the second observer ■ is substantially better than any of our experiments when segmenting only the kidney abnormalities, with an average 0.664 Dice score. Figure 5d shows four outliers for the second observer ■, three of these cases obtained a Dice score of zero and one case 0.207. The volume of these four outliers is 29, 197, 282, and 5769 mm³, three of them are below the median kidney abnormality volume in dataset B₃₀ (1421 mm³). This demonstrates the difficulty of kidney abnormality segmentation, even for experienced radiologists. The fact that we annotated multiple classes of kidney abnormalities (e.g. tumors, cysts, lesions, and masses) as a single class and the diverse patient anatomy in patients with kidney abnormalities may have contributed to the gap in performance.

Table 2 compares the Dice score obtained by previous work and our methods; the middle line separates methods that segmented kidneys without abnormalities and kidneys with abnormalities. While some methods reported Dice score for both kidneys as a single score as reported in this paper, others reported Dice scores for the left and right kidneys separately; then, we postprocessed our predictions to the same format and have a better comparison. Most of the methods trained without kidney abnormalities achieved higher Dice scores in the kidney parenchyma than those trained with kidney abnormalities (below the middle line) due to the more complex task. Although the performance of experiment 1 ■ for kidney abnormality segmentation was the lowest (0.487) among the previous work, the performance of the second observer ■ (0.664) was also below the previous work where Yu et al. [39] obtained 0.913 and Yang et al. [37] 0.802 Dice score. This disparity could be due to the fact that we grouped different types of kidney abnormalities including cysts, lesions, masses, metastases, and tumors into a single class while Yu et al. [39] and Yang et al. [37] discarded other abnormalities different than kidney tumors. Our set of kidney abnormalities is diverse in terms of volume, texture, image intensity, and location in the kidney, which makes network learning difficult.

Segmenting kidney abnormalities is challenging due to the similarity between tumors in the collecting system and kidney cysts. For instance, Figure 6 shows three cases from dataset B₃₀ where our method returned some false positives due to the similarity with tumors in the collecting system. Each case shows

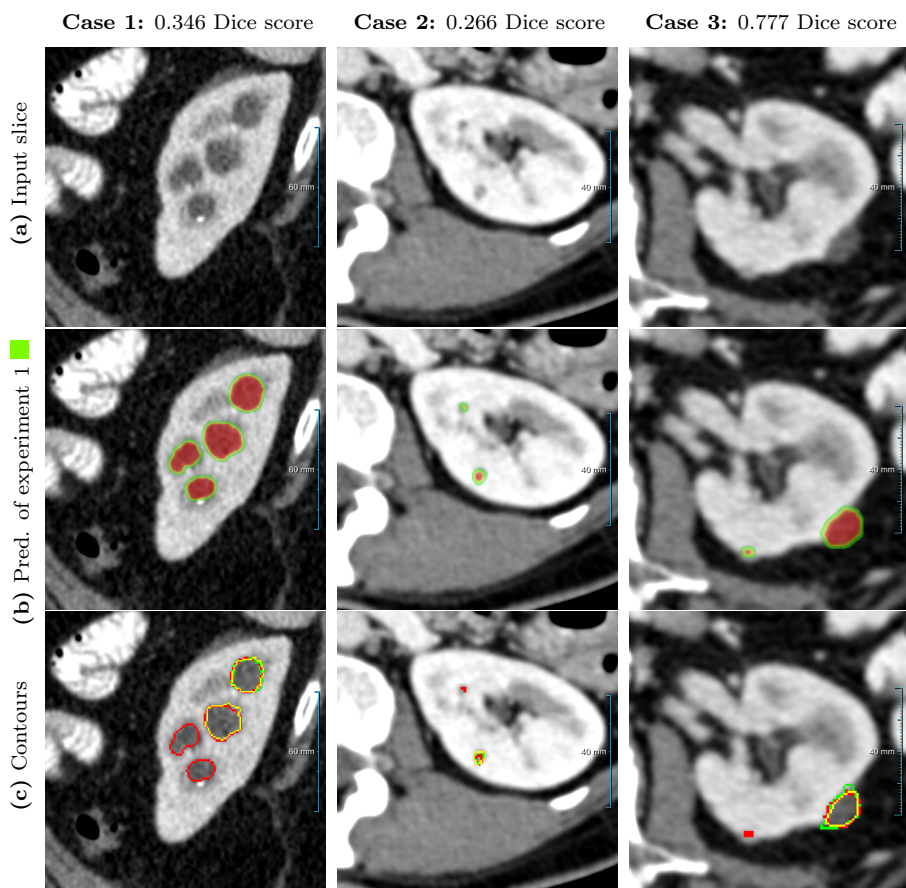


Figure 6: Comparison of three cases on the test set B_{30} between experiment 1 ■, the reference standard, and the second observer. (a) shows the original slice. (b) shows the heatmaps (predictions prior to post-processing, using a color table mapping $[0,1]$ from transparent to green to red) of experiment 1 ■. (c) shows the final predictions (red contours) of experiment 1 ■, the reference standard (green contours), and the second human observer (yellow contours). The window center and window width used for all slices were 60 HU and 360 HU.

the kidney abnormality predictions of experiment 1 ■ prior to post-processing in the second row as heatmaps. While the third row shows the post-processed segmentation, reference standard, and second observer as red, green, and yellow contours, respectively. In all three cases, a false positive by our method is present, indicated by an isolated red contour. In case 1, the false positives are abnormalities in the collecting system, which have a similar image intensity as the cysts, similarly, the second observer also segmented one of these abnormalities in the middle region. In case 2, the false positive appears as a small cyst-like region,

while in case 3, it resembles an irregular region in the kidney. Figure 7 shows a comparison of the final prediction in annotation format 1 of experiment 1 ■, the reference standard, and the second observer represented as red, green, and yellow contours, respectively. This figure shows the best and median cases of datasets B_{20} and B_{30} and the Dice score of each case computed between experiment 1 ■ and the reference standard.

A limitation of our study is that we excluded patients with unusual anatomy and with abnormalities in the collecting system.

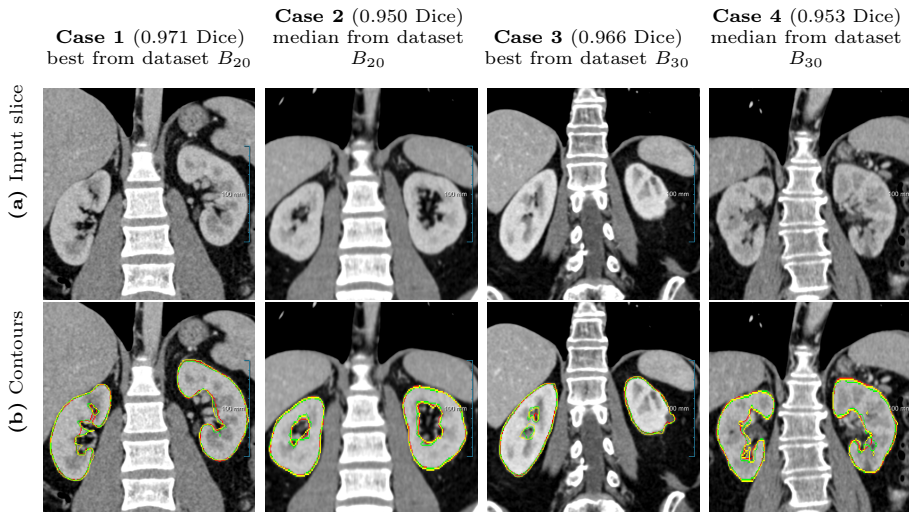


Figure 7: Comparison of four cases between experiment 1 ■, the reference standard, and the second observer on the test set B_{30} in annotation format 1. (a) shows the original slice and (b) shows the final predictions (red contours) of experiment 1 ■, the reference standard (green contours), and the second human observer (yellow contours). All the slices have a window center of 60 HU and a window width of 360 HU.

5 Conclusions

In conclusion, our ablation study and nnUNet showed that segmenting kidney abnormalities in challenging scenarios is possible, and improved performance can be achieved by an ensemble of different methods and dedicated postprocessing. The results show that our method has the potential to be a valuable tool for clinicians in detecting and monitoring kidney abnormalities. An ablation study was conducted to better understand the impact of the different modules of our method on its performance. Further research is needed to optimize the performance of experiment 1 ■ and nnUNet to test their ability to generalize to other datasets. Overall, our work contributes to the ongoing efforts to

develop accurate and reliable computer-aided diagnosis systems for detecting and quantifying renal abnormalities.

References

- [1] A. M. Ali, A. A. Farag, and A. S. El-Baz. Graph cuts framework for kidney segmentation with prior shape constraints. In *Medical Image Computing and Computer-Assisted Intervention*, pages 384–392. Springer, 2007.
- [2] P. Badura and W. Wieclawek. Calibrating level set approach by granular computing in computed tomography abdominal organs segmentation. *Applied Soft Computing*, 49:887–900, 2016.
- [3] L. Berrada, A. Zisserman, and M. P. Kumar. Smooth loss functions for deep top-k classification. *arXiv preprint arXiv:1802.07595*, 2018.
- [4] P. Bilic, P. Christ, H. B. Li, E. Vorontsov, A. Ben-Cohen, G. Kaissis, A. Szeskin, C. Jacobs, G. E. Humpire Mamani, G. Chartrand, F. Lohöfer, J. W. Holch, W. Sommer, F. Hofmann, A. Hostettler, N. Lev-Cohain, M. Drozdal, M. M. Amitai, R. Vivanti, J. Sosna, I. Ezhov, A. Sekuboyina, F. Navarro, F. Kofler, J. C. Paetzold, S. Shit, X. Hu, J. Lipková, M. Rempfler, M. Piraud, J. Kirschke, B. Wiestler, Z. Zhang, C. Hülsemeyer, M. Beetz, F. Ettliger, M. Antonelli, W. Bae, M. Bellver, L. Bi, H. Chen, G. Chlebus, E. B. Dam, Q. Dou, C.-W. Fu, B. Georgescu, X. G. i Nieto, F. Gruen, X. Han, P.-A. Heng, J. Hesser, J. H. Moltz, C. Igel, F. Isensee, P. Jäger, F. Jia, K. C. Kaluva, M. Khened, I. Kim, J.-H. Kim, S. Kim, S. Kohl, T. Konopczynski, A. Kori, G. Krishnamurthi, F. Li, H. Li, J. Li, X. Li, J. Lowengrub, J. Ma, K. Maier-Hein, K.-K. Maninis, H. Meine, D. Merhof, A. Pai, M. Perslev, J. Petersen, J. Pont-Tuset, J. Qi, X. Qi, O. Rippel, K. Roth, I. Sarasua, A. Schenk, Z. Shen, J. Torres, C. Wachinger, C. Wang, L. Weninger, J. Wu, D. Xu, X. Yang, S. C.-H. Yu, Y. Yuan, M. Yue, L. Zhang, J. Cardoso, S. Bakas, R. Braren, V. Heinemann, C. Pal, A. Tang, S. Kadoury, L. Soler, B. van Ginneken, H. Greenspan, L. Joskowicz, and B. Menze. The Liver Tumor Segmentation Benchmark (LiTS). *Medical Image Analysis*, 84: 102680, 2023. ISSN 1361-8415. doi: 10.1016/j.media.2022.102680.
- [5] N. Blau, E. Klang, N. Kiryati, M. Amitai, O. Portnoy, and A. Mayer. Fully automatic detection of renal cysts in abdominal CT scans. *International Journal of Computer Assisted Radiology and Surgery*, 13(7):957–966, 2018.
- [6] X. Chen, R. Summers, and J. Yao. FEM based 3D tumor growth prediction for kidney tumor. In *International Workshop on Medical Imaging and Virtual Reality*, pages 159–168. Springer, 2010.
- [7] G. Chlebus, A. Schenk, J. H. Moltz, B. van Ginneken, H. K. Hahn, and H. Meine. Automatic liver tumor segmentation in CT with fully convolutional neural networks and object-based postprocessing. *Nature Scientific Reports*, 8:15497, Oct. 2018. doi: 10.1038/s41598-018-33860-7.

- [8] Ö. Çiçek, A. Abdulkadir, S. S. Lienkamp, T. Brox, and O. Ronneberger. 3D U-Net: Learning dense volumetric segmentation from sparse annotation. In S. Ourselin, L. Joskowicz, M. R. Sabuncu, G. Unal, and W. Wells, editors, *Medical Image Computing and Computer-Assisted Intervention*, pages 424–432, Cham, 2016. Springer International Publishing. doi: 10.1007/978-3-319-46723-8_49. URL https://doi.org/10.1007/978-3-319-46723-8_49.
- [9] C. Farmaki, K. Marias, V. Sakkalis, and N. Graf. Spatially adaptive active contours: a semi-automatic tumor segmentation framework. *International Journal of Computer Assisted Radiology and Surgery*, 5(4):369–384, 2010.
- [10] E. Gibson, F. Giganti, Y. Hu, E. Bonmati, S. Bandula, K. Gurusamy, B. Davidson, S. P. Pereira, M. J. Clarkson, and D. C. Barratt. Automatic multi-organ segmentation on abdominal CT with dense V-Networks. *IEEE Transactions on Medical Imaging*, 37(8):1822–1834, aug 2018. doi: 10.1109/tmi.2018.2806309.
- [11] E. Gibson, W. Li, C. Sudre, L. Fidon, D. I. Shakir, G. Wang, Z. Eaton-Rosen, R. Gray, T. Doel, Y. Hu, et al. NiftyNet: a deep-learning platform for medical imaging. *Computer Methods and Programs in Biomedicine*, 158: 113–122, 2018.
- [12] X. Glorot and Y. Bengio. Understanding the difficulty of training deep feed-forward neural networks. In *International conference on artificial intelligence and statistics*, pages 249–256, 2010.
- [13] M. Haghghi, S. K. Warfield, and S. Kurugol. Automatic renal segmentation in DCE-MRI using convolutional neural networks. In *IEEE International Symposium on Biomedical Imaging*, pages 1534–1537, Apr. 2018. doi: 10.1109/ISBI.2018.8363865.
- [14] X. Han. Automatic liver lesion segmentation using a deep convolutional neural network method. *arXiv:1704.07239*, 2017. doi: 10.1002/mp.12155.
- [15] F. Heckel, M. Schwier, and H.-O. Peitgen. Object-oriented application development with MeVisLab and Python. *Lecture Notes in Informatics (Informatik 2009: Im Focus das Leben)*, 154:1338–1351, 2009.
- [16] M. P. Heinrich, O. Oktay, and N. Bouteldja. OBELISK-Net: Fewer layers to solve 3D multi-organ segmentation with sparse deformable convolutions. *Medical Image Analysis*, 54:1–9, May 2019. ISSN 1361-8423. doi: 10.1016/j.media.2019.02.006.
- [17] N. Heller, F. Isensee, K. H. Maier-Hein, X. Hou, C. Xie, F. Li, Y. Nan, G. Mu, Z. Lin, M. Han, G. Yao, Y. Gao, Y. Zhang, Y. Wang, F. Hou, J. Yang, G. Xiong, J. Tian, C. Zhong, J. Ma, J. Rickman, J. Dean, B. Stai, R. Tejpaul, M. Oestreich, P. Blake, H. Kaluzniak, S. Raza, J. Rosenberg, K. Moore, E. Walczak, Z. Rengel, Z. Edgerton, R. Vasdev, M. Peterson, S. McSweeney,

- S. Peterson, A. Kalapara, N. Sathianathen, N. Papanikolopoulos, and C. Weight. The state of the art in kidney and kidney tumor segmentation in contrast-enhanced CT imaging: Results of the KiTS19 challenge. *Medical Image Analysis*, 67:101821, 2021.
- [18] F. Isensee, P. F. Jaeger, S. A. A. Kohl, J. Petersen, and K. H. Maier-Hein. nnU-Net: a self-configuring method for deep learning-based biomedical image segmentation. *Nature methods*, 2020. ISSN 1548-7091. doi: 10.1038/s41592-020-01008-z.
- [19] P. Jackson, N. Hardcastle, N. Dawe, T. Kron, M. Hofman, and R. J. Hicks. Deep learning renal segmentation for fully automated radiation dose estimation in unsealed source therapy. *Frontiers in oncology*, 8:215, 2018.
- [20] R. Kaur, M. Juneja, and A. Mandal. A hybrid edge-based technique for segmentation of renal lesions in CT images. *Multimedia Tools and Applications*, 78(10):12917–12937, 2019.
- [21] F. Khalifa, A. Soliman, A. Elmaghraby, G. Gimelfarb, and A. El-Baz. 3D kidney segmentation from abdominal images using spatial-appearance models. *Computational and mathematical methods in medicine*, 2017, 2017.
- [22] D.-Y. Kim and J.-W. Park. Computer-aided detection of kidney tumor on abdominal computed tomography scans. *Acta Radiologica*, 45(7):791–795, 2004.
- [23] D. Kingma and J. Ba. Adam: A method for stochastic optimization. *arXiv preprint arXiv:1412.6980*, 2014.
- [24] A. Kutikov and R. G. Uzzo. The RENAL nephrometry score: a comprehensive standardized system for quantitating renal tumor size, location and depth. *Journal of Urology*, 182(3):844–853, 2009.
- [25] D.-T. Lin, C.-C. Lei, and S.-W. Hung. Computer-aided kidney segmentation on abdominal CT images. *IEEE Transactions on Information Technology in Biomedicine*, 10(1):59–65, 2006.
- [26] M. G. Linguraru, J. Yao, R. Gautam, J. Peterson, Z. Li, W. M. Linehan, and R. M. Summers. Renal tumor quantification and classification in contrast-enhanced abdominal CT. *Pattern Recognition*, 42(6):1149–1161, 2009.
- [27] J. Lu, J. Chen, J. Zhang, and W. Yang. Segmentation of kidney using CV model and anatomy priors. In *Medical Imaging, Parallel Processing of Images, and Optimization Techniques*, volume 6789 of *Proceedings of the SPIE*, page 678911, 2007.
- [28] O. Ronneberger, P. Fischer, and T. Brox. U-Net: Convolutional networks for biomedical image segmentation. In *Medical Image Computing and Computer-Assisted Intervention*, volume 9351 of *Lecture Notes in Computer Science*, pages 234–241, 2015.

- [29] K. Sharma, C. Rupprecht, A. Caroli, M. C. Aparicio, A. Remuzzi, M. Baust, and N. Navab. Automatic segmentation of kidneys using deep learning for total kidney volume quantification in autosomal dominant polycystic kidney disease. *Nature Scientific Reports*, 7(1):2049, 2017. doi: 10.1038/s41598-017-01779-0.
- [30] R. L. Siegel, K. D. Miller, and A. Jemal. Cancer statistics, 2019. *CA: A Cancer Journal for Clinicians*, 69(1):7–34, 2019.
- [31] A. Skalski, K. Heryan, J. Jakubowski, and T. Drewniak. Kidney segmentation in CT data using hybrid Level-Set method with ellipsoidal shape constraints. *Metrology and Measurement Systems*, 24(1):101–112, 2017. doi: 10.1515/mms-2017-0006.
- [32] A. Taha, P. Lo, J. Li, and T. Zhao. Kid-Net: convolution networks for kidney vessels segmentation from CT-volumes. In *Medical Image Computing and Computer-Assisted Intervention*, pages 463–471. Springer, 2018.
- [33] J. Tompson, R. Goroshin, A. Jain, Y. LeCun, and C. Bregler. Efficient object localization using convolutional networks. In *Computer Vision and Pattern Recognition*, pages 648–656, 2015.
- [34] D. Turco, M. Valinoti, E. M. Martin, C. Tagliaferri, F. Scolari, and C. Corsi. Fully automated segmentation of polycystic kidneys from noncontrast computed tomography: A feasibility study and preliminary results. *Academic Radiology*, 25(7):850–855, 2018.
- [35] Y. Wang, Y. Zhou, P. Tang, W. Shen, E. K. Fishman, and A. L. Yuille. Training multi-organ segmentation networks with sample selection by relaxed upper confident bound. In *Medical Image Computing and Computer-Assisted Intervention*, pages 434–442. Springer, 2018.
- [36] W. Wieclawek. 3D marker-controlled watershed for kidney segmentation in clinical CT exams. *Biomedical Engineering Online*, 17(1):26, 2018.
- [37] G. Yang, G. Li, T. Pan, Y. Kong, J. Wu, H. Shu, L. Luo, J. Dillenseger, J. Coatrieux, L. Tang, and X. Zhu. Automatic segmentation of kidney and renal tumor in CT images based on 3D fully convolutional neural network with pyramid pooling module. In *International Conference on Pattern Recognition*, pages 3790–3795, Aug. 2018. doi: 10.1109/ICPR.2018.8545143.
- [38] U. Yoruk, B. A. Hargreaves, and S. S. Vasanawala. Automatic renal segmentation for MR urography using 3D-GrabCut and random forests. *Magnetic Resonance in Medicine*, 79(3):1696–1707, 2018.
- [39] Q. Yu, Y. Shi, J. Sun, Y. Gao, J. Zhu, and Y. Dai. Crossbar-Net: A novel convolutional neural network for kidney tumor segmentation in CT images. *IEEE Transactions on Image Processing*, 28(8):4060–4074, 2019. ISSN 1057-7149. doi: 10.1109/TIP.2019.2905537.

- [40] Y. Zheng, D. Liu, B. Georgescu, D. Xu, and D. Comaniciu. Deep learning based automatic segmentation of pathological kidney in CT: Local versus global image context. In *Advances in Computer Vision and Pattern Recognition*, pages 241–255. Springer, Cham, 2017. doi: 10.1007/978-3-319-42999-1_14.